Measuring optical properties of clear and turbid media with broadband spectral interferometry

Speets, Peter N.A.; Kalkman, Jeroen

DOI
10.1364/AO.488543

Publication date
2023

Document Version
Final published version

Published in
Applied Optics

Research Article Vol. 62, No. 16 / 1 June 2023 / Applied Optics 4349

applied optics

Measuring optical properties of clear and turbid media with broadband spectral interferometry

PETER N. A. SPEETS AND JEROEN KALKMAN*

Department of Imaging Physics, Delft University of Technology, Lorentzweg 1, 2628 CJ, Delft, The Netherlands
**j.kalkman@tudelft.nl*

Received 23 February 2023; revised 19 April 2023; accepted 21 April 2023; posted 21 April 2023; published 25 May 2023

The group index, n_g, group velocity dispersion (GVD), and scattering attenuation coefficient, μ_s, were measured for dilutions of glycerol, ethanol, and Intralipid 20% with water. Experiments were performed with a supercontinuum laser based Mach–Zehnder spectroscopic interferometry setup for wavelengths between 400 and 930 nm. All optical properties could be retrieved from a single calibrated measurement of the interference spectrum. Scattering attenuation was determined from the envelope of the interference. The group index and GVD were retrieved from the unwrapped spectral phase. It was found that the group indices of glycerol and ethanol dilutions are in accordance with the Lorentz–Lorenz mixing formula. The scattering attenuation matches well to a semi-empirical model based on the Twerksy effective packing fraction.

https://doi.org/10.1364/AO.488543

1. INTRODUCTION

Optical characterization of liquids has been done for centuries [1] and is used for studying both fluid dynamic processes and fluid composition. The non-invasive nature of light makes it particularly suitable for sensing fluid optical properties such as attenuation, caused by both absorption and scattering, and the refractive index. Measurement of the attenuation coefficient is, among others, used for characterization of human milk [2], blood [3], or quality control of water [4] or dairy products [5]. Likewise, refractive index sensing can provide valuable information about a sample, for example, to distinguish blood groups [6], glucose content [7], or water salinity [8]. The dispersion of the refractive index can be considered as valuable additional information. Similar to the refractive index, it was used to determine the concentration of glucose [9,10], salinity [9], or the amount of hemoglobin in red blood cells [11].

An established technique to measure the attenuation coefficient of a sample is by means of double integrating spheres [5,12]. Although this can be used for spectral attenuation measurements, measurement of the refractive index of the sample is not possible since all path length information is lost with this technique. In turn, very sensitive techniques to measure the refractive index are by means of tapered optical fibers [13] or microresonators [14,15]. An advantage of these sensors is that they can be functionalized for high specificity [13,16]. However, these techniques are not compatible with simultaneous measurement of the attenuation coefficient.

An old, but widely used, technique to measure the refractive index is by measurement of the critical or Brewster angle. With this method, it is possible to simultaneously determine the refractive index and attenuation coefficient [17–19]. For these methods, scattering needs to be taken into account in the Fresnel equations [20]. However, the critical angle can be difficult to accurately determine for absorbing or strongly scattering media [21,22]. In addition, the maximum refractive index that can be measured is limited by the refractive index of the prism or half cylinder used in the measurement. Moreover, multiple wavelengths cannot be measured simultaneously and need to be measured consecutively.

The attenuation coefficient and refractive index can also be measured with optical coherence tomography (OCT). In the case of reflection OCT, the signal attenuation coefficient of the sample can be fitted to the exponential decay of the intensity with respect to the optical path length (OPL) [3,23–26]. The dispersion of the refractive index can be obtained with reflection OCT by fitting the phase to the PSF of a strong reflector or speckle [27]. A second method to measure the refractive properties with reflection OCT is with the spatial displacement between the Fourier transform of different parts of the measured spectrum [28]. Obviously, the need for backscattering requires a turbid medium and is not applicable to transparent samples.

With transmission OCT, the attenuation coefficient, group index, and group velocity dispersion (GVD) can be measured simultaneously. If the intensity of both arms of the interferometer is measured separately, the attenuation coefficient can be measured straightforwardly from the transmission. The transmission of a sample can also be measured from the height of the OPL peak [10] or with a low pass filter on the interference signal [29]. The group index and GVD are obtained from the phase of the interference signal [10,30]. The combined measurement of attenuation and group index can even be spatially mapped in 3D [31].

In this work, we applied broadband transmission OCT to simultaneously measure the wavelength dependence of the group index n_g, GVD, and optical attenuation of clear fluids and turbid media in a single shot. The large bandwidth allows for a highly accurate determination of n_g and GVD. This setup was used to measure the group index and GVD of glycerol, ethanol, and Intralipid at different concentrations. In addition, the scattering coefficient of suspensions of Intralipid 20% dilutions was measured. The refractive index and attenuation coefficient were compared to models based on literature values of the fluid components.

2. THEORY

A. Interferometric Signal

To obtain both amplitude and phase information, we use spectral interferometry, as schematically shown in Fig. 1. The light from the source, with wavenumber $k = 2\pi/\lambda$ and spectral density $S(k)$, passes a beam splitter with intensity splitting ratio α. We assume ballistic light interaction with the sample. Hence, the intensity in the sample is exponentially attenuated by absorption, characterized by $\mu_a(k)$, and scattering, characterized by $\mu_s(k)$ over a length L. The phase of the signal is determined by the refractive index $n(k)$ of the sample. The intensity as measured with the spectrometer $I_{\text{tot}}(k)$ can be considered as the sum of the intensity of the sample arm $I_{\text{sam}}(k)$, the reference arm $I_{\text{ref}}(k)$, and the interference $I_{\text{int}}(k)$:

$$I_{\text{tot}}(k) = I_{\text{sam}}(k) + I_{\text{ref}}(k) + I_{\text{int}}(k). \tag{1}$$

The light through the sample is recombined with the reference by a second beam splitter with intensity splitting ratio α. Assuming negligible absorption, the detected field from the sample arm is

$$E_{\text{sam}}(k) = \sqrt{S(k)}\sqrt{\alpha(1-\alpha)}\,\mathrm{e}^{-\frac{1}{2}\mu_s(k)L}\,\mathrm{e}^{in(k)kL}. \tag{2}$$

With the reference field propagating in air, i.e., $n = 1$, the detected field from the reference arm is

$$E_{\text{ref}}(k) = \sqrt{S(k)}\sqrt{(1-\alpha)\alpha}\,\mathrm{e}^{ik\delta}. \tag{3}$$

Here δ is the difference in path length in air between the sample arm and reference arm. Combining Eqs. (2) and (3) and removing the constant intensities results in the interference intensity

$$I_{\text{int}}(k) = 2S(k)\alpha(1-\alpha)\mathrm{e}^{-\frac{1}{2}\mu_s(k)L}\cos(k\delta - n(k)kL). \tag{4}$$

The cosine part of the interference term of Eq. (4) consists of a phase delay due to the refractive index of the sample and a constant phase offset given by the path length difference δ. The OPL distribution of the transmitted light is given by the inverse Fourier transform of the interference intensity.

The phase of the cosine term $\phi = (k\delta - n(k)kL)$ varies with k and can be obtained from the interference intensity using a Hilbert transform, denoted by $\mathcal{H}$. The Hilbert transform rotates the signal with $-\frac{1}{2}\pi$ in the complex plane and inverts the sign of the negative frequencies of the Fourier transform of the signal. This transforms the cosine term in a sine term. The complex-valued interference spectrum $\tilde{I}_{\text{int}}(k)$ can then be obtained by combining Eq. (4) with the Hilbert transform as

$$\tilde{I}_{\text{int}}(k) = I_{\text{int}}(k) + i\mathcal{H}\{I_{\text{int}}(k)\}. \tag{5}$$

The phase $\phi(k)$ of the interference is then obtained from Eq. (5) in the conventional way as

$$\phi(k) = \arctan\left(\frac{\mathrm{Im}\{\tilde{I}_{\text{int}}(k)\}}{\mathrm{Re}\{\tilde{I}_{\text{int}}(k)\}}\right). \tag{6}$$

Similarly, the envelope of the interference spectrum can be calculated with the absolute value of Eq. (5). The intensity transmission with respect to a calibration sample can be obtained by taking the ratio of the envelopes of the interference signal. This is given by

$$T(k) = \frac{\left|\tilde{I}_{\text{int}}^{\text{sam}}(k)\right|^2}{\left|\tilde{I}_{\text{int}}^{\text{cal}}(k)\right|^2}. \tag{7}$$

Here $T(k)$ is the transmission of the sample, and $\tilde{I}_{\text{int}}^{\text{sam}}(k)$ and $\tilde{I}_{\text{int}}^{\text{cal}}(k)$ the complex interference spectrum of the sample of interest and the spectrum of a calibration sample, respectively. The attenuation follows from $T(k) = \exp(-\mu(k)L)$.

B. Parametrization of the Refractive Index

In the visible and near infrared regions, which are far from molecular absorption peaks, the refractive index $n(k)$ is well described by the Cauchy equation [32]. This is a polynomial parametrization that is monotonically decreasing with

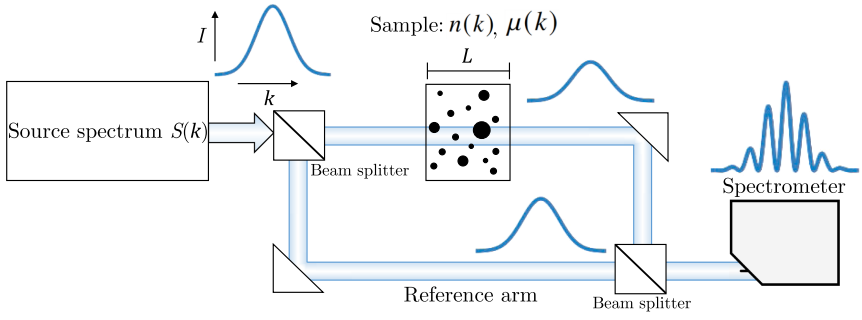

Fig. 1. Schematic overview of the spectral interferometry setup. Light from a broadband source is split into a reference arm and a sample arm. The amplitude through the sample arm is attenuated by the sample. The phase of the light through the sample arm is delayed by the refractive index of the sample.

wavelength. With the Cauchy equation the interferometric phase is given by

$$\phi(k) = n(k)Lk + 2\pi N = \sum_m \phi_m k^m, \tag{8}$$

with N the number of full wavelengths λ that fit into the distance L and ϕ_m a set of empirical parameters. The phase $\phi(k)$ is used to calculate the group index n_g by

$$n_g = n + k\frac{dn}{dk} = L^{-1}\frac{d\phi}{dk} \tag{9}$$

and the GVD

$$\text{GVD} = \frac{2}{c^2}\frac{dn(k)}{dk} + \frac{k}{c^2}\frac{d^2n(k)}{dk^2} = \frac{1}{Lc^2}\frac{d^2\phi(k)}{dk^2}, \tag{10}$$

with c the speed of light in vacuum. Therefore, when the phase $\phi(k)$ is determined from the complex-valued interference signal of Eq. (4), the group refractive index and GVD of the sample can be determined.

C. Refractive Index of Molecular Mixtures

The refractive index of a mixture of molecular components is, for many mixtures, well approximated by the Arago–Biot equation [33]. For a two component mixture, the Arago–Biot approximation for the refractive index of the mixture is

$$n_{\text{mix}}(k) = f_v n_1(k) + (1 - f_v)n_2(k), \tag{11}$$

with f_v the volume fraction of the solute and $n_1(k)$ and $n_2(k)$ the refractive indices of components 1 and 2, respectively. The Arago–Biot equation holds well for mixtures where the mass density of the mixture is the weighted average of the two components. For mixtures where the mass density ρ_{mix} depends nonlinearly on the volume fraction f_v, e.g., due to strong inter-molecular interactions, an improved model is the Lorentz–Lorenz mixing formula [34,35]

$$\frac{n_{\text{mix}}^2(k) - 1}{n_{\text{mix}}^2(k) + 2}\frac{f_v\rho_1 + (1 - f_v)\rho_2}{\rho_{\text{mix}}(f_v)} = v_f\frac{n_1^2(k) - 1}{n_1^2(k) + 2} + (1 - v_f)\frac{n_2^2(k) - 1}{n_2^2(k) + 2}. \tag{12}$$

Here $n_{\text{mix}}(k)$ is the refractive index of the mixture, and ρ_1 and ρ_2 are the mass densities of components 1 and 2, respectively. The Lorentz–Lorenz mixing formula explicitly incorporates the mass density of the mixture $\rho_{\text{mix}}(f_v)$, which may nonlinearly depend on the volume fraction f_v.

D. Attenuation Coefficient of a Scattering Medium

For suspensions with a wide particle size distribution, e.g., Intralipid, the wavelength dependence of the scattering coefficient of Intralipid can be described with a power law [36]:

$$\mu_s = A\lambda^{-\alpha}, \tag{13}$$

with A a proportionality constant, λ the wavelength, and α an empirical parameter. For particles in the Rayleigh regime, $\alpha = 4$.

Dependent scattering effects on the attenuation coefficient can be modeled with the Twersky effective packing fraction W [37,38], which is defined as

$$W = f_v\left(\frac{(1 - f_v)^{p+1}}{(1 + f_v(p - 1)^{p-1})}\right), \tag{14}$$

with p the packing dimension, which is exactly three for monodisperse hard sphere particles. The packing dimension decreases for particles that can be packed more efficiently than hard spheres. Therefore, it is expected that $p < 3$ for anisotropic particles or polydisperse particle size distributions. The dependent scattering coefficient can be modeled with the effective packing fraction as

$$\mu_s(\lambda) = A\lambda^{-\alpha}W = A\lambda^{-\alpha}f_v\left(\frac{(1 - f_v)^{p+1}}{1 + f_v(p - 1)^{p-1}}\right). \tag{15}$$

3. METHODS AND MATERIALS

A. Experimental Setup

A schematic of the experimental setup is shown in Fig. 2. The light source is a supercontinuum laser (EVO EUL-10, NKT) that has a collimator at the end of its fiber. The laser is operated at maximum power to emit light with optimal stability and to obtain the maximum spectral bandwidth. The infrared part of the light is filtered from the spectrum by a dichroic mirror (DMLP950, Thorlabs) that reflects wavelengths between 400 and 950 nm. Light within the visible wavelength band is attenuated by two neutral density filters (ND4A and ND10A, Thorlabs). Subsequently, the light is split into the reference arm and the sample arm by a 50-50 beam splitter (BS013, Thorlabs) for the glycerol and ethanol measurements and a 10-90 beam splitter (BS025, Thorlabs) for the Intralipid measurements, directing more power to the sample to compensate for the lower transmission. The collimated beam passes through the sample without any focusing.

In the reference arm, a neutral density filter (NDC-100C-4M, Thorlabs) is placed, but set to the transparent area for glycerol and ethanol measurements. For Intralipid measurements, the filter wheel was set such that the intensity of the

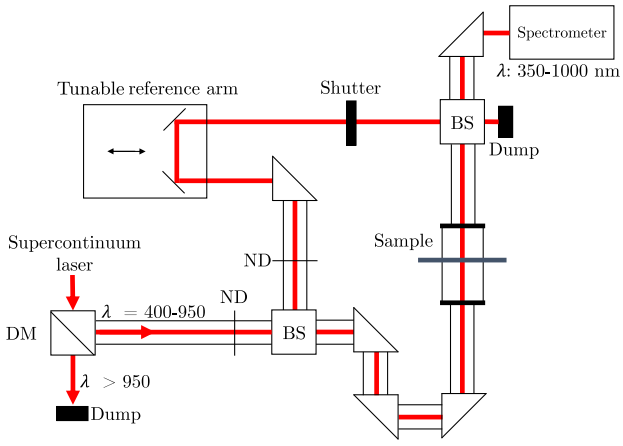

Fig. 2. Overview of the broadband spectral interferometry setup. DM, BS, ND indicate the dichroic mirror, beam splitter, and neutral density filter, respectively.

reference arm was close to the intensity of light transmitted through the sample. The light is recombined with a 50-50 beam splitter (BS013, Thorlabs). The recombined beam passes through an iris (SM05D5D, Thorlabs) set at the smallest diameter of 0.7 mm. The spectrum is measured with a 2046 pixel spectrometer (FX VIS-NIR, Ocean Optics). When feasible, the optical components were connected with a cage system. The system was enclosed in a shielded environment to avoid air current variations and ensure safe operation.

B. Sample Preparation and Methods

A cuvette with an inner width of 500 μm (106-0.50-40, Hellma) was used for measurements with glycerol dilutions. The lower viscosity of ethanol allowed for the use of a larger flow cell of 1000 μm (45/Q/1, Starna). Due to the high scattering of the undiluted Intralipid, a thinner 200 μm flow cell (45/Q/0.2, Starna) was used that still transmits for these concentrations.

The glycerol (M152-1L, Amresco), ethanol (99.8% 1L, Riedel-de Haën), and Intralipid (I141-100ML, Sigma-Aldrich) were diluted with demineralized water (Milliq 15 MΩcm). For the glycerol measurement, the cuvette was cleaned with isopropanol between each measurement. Before each measurement on ethanol or Intralipid dilutions, the previous sample was flushed out by air and demineralized water. The mixture was introduced to the flow cell by a BD10 Luer-Lock syringe, while the flow cell was maintained at the exact same location. The setup was calibrated with phase and attenuation measurements of demineralized water.

The OPL difference between the reference arm and the sample arm was set between 50 and 100 μm, well below the maximum OPL difference of 340 μm for this setup. The exposure time of the spectrometer was varied between each measurement such that each measurement could use a large portion of the dynamic range of the spectrometer. This was 100 μs for both glycerol and ethanol measurements, and their calibration measurements. For the Intralipid, this was 1 ms for the lowest volume fraction to 5 ms for the highest volume fraction. For calibration of the Intralipid measurements, the exposure time of the spectrometer was set to 200 μs. The number of spectra ranged from 2000 to 20,000 such that the noise in the light source, the shot noise, and the electronic noise were properly averaged out. The background spectrum was measured by blocking both arms and was subtracted from each measured spectrum for each different integration time.

C. Data Analysis

The analysis of the spectrum of a measurement is summarized in the flow chart shown in Fig. 3 with the first step the measured spectrum $I_{\text{measured}}(\lambda)$. As an example, the analysis steps of the spectrum of a measurement of an Intralipid dilution of 2.27 vol.% in water is shown in Fig. 4.

In the first step, a wavelength range is selected in which there is sufficient signal; determined by the spectrum of the light source, dichroic mirror, the response of the grating and sensor in the spectrometer, and the attenuation of the sample. The resulting spectrum is $I_{\text{tot}}(\lambda)$. For the glycerol and ethanol dilutions, wavelengths between 400 and 930 nm were used. For

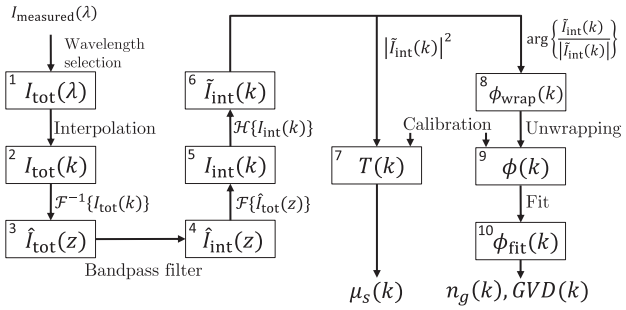

Fig. 3. Flow chart of the analysis steps.

low wavelengths, the measurements of the Intralipid dilutions were strongly attenuated. Therefore, the lower wavelength bound was increased for higher volume fractions of Intralipid. For volume fractions between 2.27 and 13.62 vol.%, the lower bound was set to 460 nm; for volume fractions between 15.59 and 18.16 vol.%, this was 480 nm; and for the volume fraction of 20.43 vol.% soy oil in water and undiluted Intralipid (22.7 vol.%), this was 500 nm.

In the second step, the measured spectrum is interpolated from the wavelength domain to linear wavenumbers with the Scipy [39] interp1d function. The interpolated interference spectra of the Intralipid dilution and its reference water measurement are shown in Fig. 4(a).

In the third step, the spectral data are inverse Fourier transformed to the spatial domain. The absolute value of the inverse Fourier transform is shown in Fig. 4(b). The peaks around 85 μm correspond to the OPL difference between the reference arm and sample arm. The shape of these peaks is determined by the envelope of the interference spectrum and the dispersion caused by the sample and the optical elements.

In the fourth step, the Fourier transform of the pure interference term, as shown in Eq. (4), is obtained by applying a bandpass filter to the signal. The boundaries of the bandpass filter are indicated with dashed lines in Fig. 4(b), with the colors indicating the edge for the different substances. Because the Fourier peak is not symmetric, the bounds of the bandpass filter are calculated for the left and right sides separately. The bounds are taken to be eight times the distance between the position of the maximum value and the position at half the maximum value of the envelope corrected peak. For the measurements shown in Fig. 4(b), the lower bound is set at 68 μm. The upper bound is set for the Intralipid measurement to 97 μm, indicated by the blue line. For the water calibration, this it set at 119 μm, as indicated with the red line.

In step 5, the signal is Fourier transformed back to the spectral domain. The filtered spectral signal is shown in Fig. 4(c). In step 6, the complex interference $\tilde{I}(k)$ is determined with the Hilbert transform according to Eq. (5). In step 7, the envelope of the interference is calculated with the absolute value of the complex interference of the filtered signal $|\tilde{I}_{\text{int}}(k)|$. The envelopes of the interference of the Intralipid dilution and water are indicated with green and orange, respectively in Fig. 4(c). The transmission is calculated from the envelope according to Eq. (7) and a calibration measurement of water.

The phase and amplitude of the Hilbert transform can have a fringe pattern near the edges. This can be seen in Fig. 4(c) for

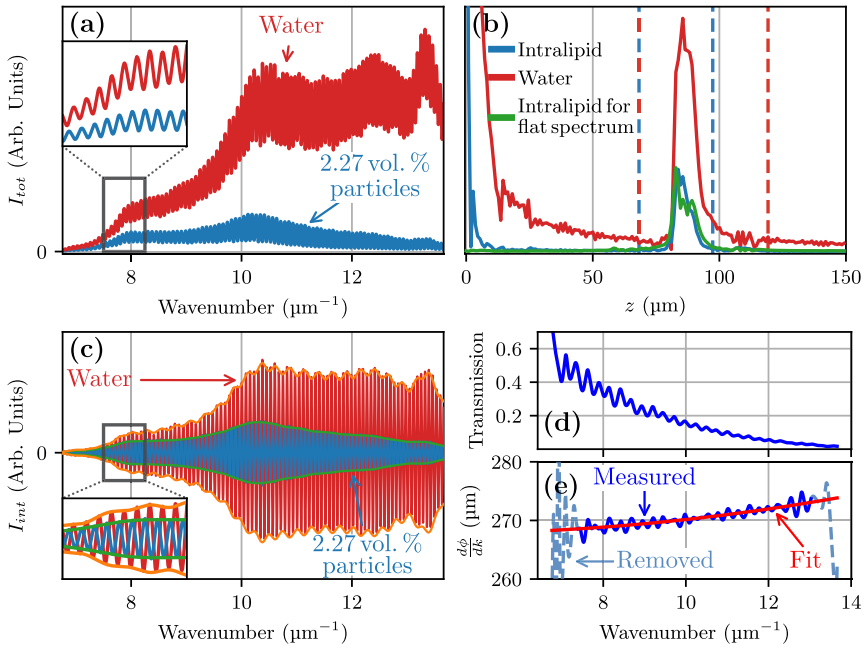

Fig. 4. (a) Measured spectra of water and an Intralipid dilution with 2.27 vol.% oil particles in water. (b) Fourier transform of aforementioned spectra. The dashed vertical lines indicate the bandpass filter. (c) Filtered interference. (d) Transmission of the Intralipid and (e) derivative of the phase $\phi(k)$ of Intralipid.

wavenumbers smaller than 7 μm^{-1}. Therefore, the envelope of the interference spectrum is calculated only for a spectral region 100 nm smaller than the full wavelength range. The transmission is calculated according to Eq. (7) and shown for 2.27 vol.% soy oil in Fig. 4(d).

In step 8, the phase $\phi(k)$ is obtained from the complex interference $\tilde{I}_{\text{int}}(k)$. First, the interference spectrum is divided by the envelope of the interference. The Fourier transform of this reshaped interference is shown in green in Fig. 4(b). Without the envelope, the Fourier spectrum has the typical shape of an up-chirped signal. The phase is calculated by taking the complex angle of the complex-valued interference spectrum of Eq. (6). It is possible to obtain the phase from a Hilbert transform of the interference of step 3. However, isolating the interference frequencies and normalizing the signal greatly reduces the fringe patters that can be seen in Fig. 4(e).

In step 9, this phase is unwrapped. After unwrapping, the measured spectral phase $\phi(k) = \phi_m(k)$ needs to be compensated for the system dispersion. This is done with a calibration measurement with demineralized water. The phase of the sample ϕ_{sample} is

$$\phi_{\text{sample}}(k) = \phi_m(k) - \phi_c(k) + n_{\text{water}}(k)kL, \qquad (16)$$

with $\phi_m(k)$ the measured phase of the medium, $\phi_c(k)$ the phase of the water calibration measurement, and $n_{\text{water}}(k)kL$ the phase of the water. The refractive index of water $n_{\text{water}}(k)$ is taken from Daimon and Masumura [40] for 20°C. The unwrapped phase of the same measurement with diluted Intralipid is shown in Fig. 4(e).

The group index and GVD are proportional to, respectively, the first and second derivatives of the phase with respect to the wavenumber k. To obtain these derivatives, the phase is fitted in step 10 with the polynomial of Eq. (8). For the glycerol and ethanol measurements, a fourth order polynomial was fitted to the phase with the first and last 200 elements removed from the total of 8192. For Intralipid, the phase is fitted with a third order polynomial, and the first and last 750 elements were removed from the measured spectrum. The elements that were retained are shown in dark blue in Fig. 4(e). The reduction of the spectral range was done to avoid edge effects on the phase estimation, as shown in light blue in Fig. 4(e). The lower order polynomial for Intralipid means that the measured GVD was assumed to be at most linearly dependent on wavenumber.

The wavenumber dependent group index and GVD are calculated using Eqs. (9) and (10) from the polynomial fit of the sample phase.

The dependence of the group index and GVD on the mixture ratio of glycerol and ethanol was parameterized with a parabola and with a linear dependence for Intralipid. The confidence interval was given by the standard error of the fit parameters. The confidence interval of the scattering attenuation measurements was determined from the standard deviation of the fit parameters A, α, and p of Eq. (15).

D. Optical Reference Data

The group index and GVD of glycerol and ethanol are compared with literature data and the Lorentz–Lorenz mixing formula. The refractive indices of water, glycerol, and ethanol were taken from Daimon and Masumura [40], Gupta *et al.* [41], and Kedenburg *et al.* [42], respectively. However, Gupta *et al.* measured the refractive index of glycerol only for wavelengths lower than 710 nm. Therefore the dispersion formula, as reported by Gupta *et al.*, was extrapolated to higher wavelengths.

The refractive index of the water–glycerol and water–ethanol mixtures is dependent on the mixing ratio and the mass density. The mass density as a function of volume fraction of glycerol in water is taken from Volk and Kähler [43] and for ethanol in water from Danahy *et al.* [44]. With these data, the phase index for the mixture was calculated with the Lorentz–Lorenz Eq. (12). The expected group index and GVD were calculated with Eqs. (9) and (10).

4. RESULTS

A. Refractive Properties of Undiluted Samples

In Fig. 5, the measured group index and GVD of pure glycerol, ethanol, and Intralipid are shown. The measured group index of ethanol follows the expected Cauchy relationship with wavenumber k. The measured group index of glycerol is slightly higher than reported by Gupta *et al.* [41]. For pure Intralipid, the scattering attenuation for wavenumbers higher than $11.5\mu m^{-1}$ (550 nm) was too high to reliably measure the phase of the interference spectrum. For Intralipid, no reliable literature data are available. For the GVD, the data of the ethanol measurements agree well with the literature values by Kedenburg *et al.* [42]. For glycerol, the GVD at the center wavenumber matches the literature values reasonably well. However, the measured wavenumber dependence is much stronger than reported by Gupta *et al.*

The dependence of the group index and GVD of glycerol and ethanol on the mixing ratio at various wavelengths is shown in Fig. 6. In Fig. 6(a), the measured group index of the glycerol dilutions matches the prediction by Eq. (12). In Fig. 6(b), the mixing ratio dependence of the GVD is linear for all glycerol–water mixtures. This is expected, as the mass density of glycerol–water mixtures is an almost linear function of the mixing ratio [43] and hence gives a GVD that depends almost linearly on the mixing ratio according to Eq. (12). The results are in good agreement with the literature values, especially at the center of the spectrum where the phase estimation is most accurate.

The group index of ethanol is shown in Fig. 6(c). For ethanol, the dependence of the group index on the mixing ratio is nonlinear. In fact, the group index of ethanol reaches a maximum at a volume fraction of 75 vol.%. The nonlinear behavior of the group index is due to the nonlinear relationship of the mass density with the mixing ratio. This is caused by the strong

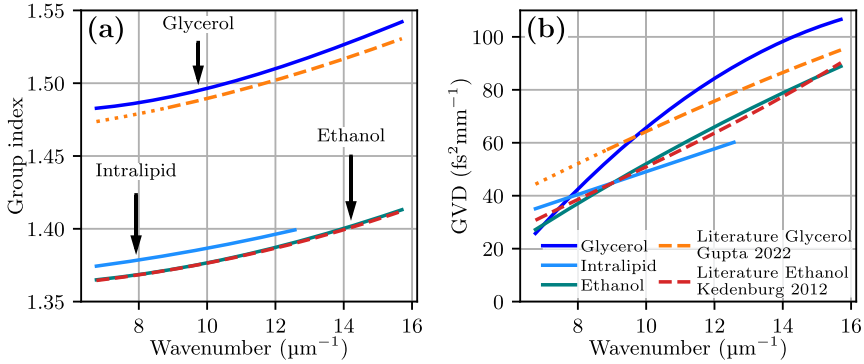

Fig. 5. Wavenumber dependence of the measured (a) group index and (b) GVD compared to literature. Interpolated literature values are indicated with a dashed line, extrapolated values with a dotted line.

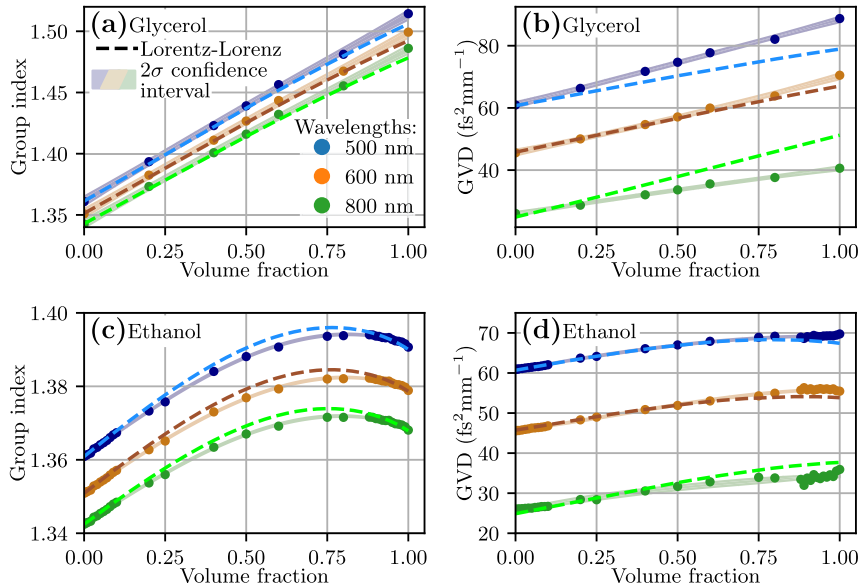

Fig. 6. Group index and GVD of glycerol and ethanol mixtures as function of volume fraction at various wavelengths.

hydrogen bond interactions in the mixture, not only between ethanol and water molecules, but also among molecules of the same species [45].

In contrast to the glycerol–water mixtures, the mixing ratio dependence of the GVD of ethanol–water mixtures is nonlinear. This follows from the prediction of Eq. (12) and the mixing ratio dependence of the mass density of ethanol–water mixtures [44]. Figure 6(d) shows that the GVD at 800 nm monotonically increases with volume fraction. For wavelengths 500 and 600 nm, the GVD obtains a maximum at high ethanol concentrations.

The absorption of glycerol ($<0.25\ \mathrm{mm}^{-1}$ at 589 nm [46]) and ethanol ($\sim 0.1\ \mathrm{m}^{-1}$ at 589 nm [42]) was too small to reliably measure with the path length of the flow cell used in this experiment.

B. Optical Properties of Particle Suspensions

The concentration dependence of the group index and GVD of Intralipid is shown in Fig. 7. The group index of the Intralipid mixtures increases monotonically with volume fraction. The nonpolar soy oil droplets in an Intralipid emulsion are hydrophobic. It is expected that these droplets have very small interactions with the solvent at the molecular level. Therefore, the mass density and hence the group index and GVD are a linear function of the mixing ratio.

The low transmission and smaller channel sizes of the Intralipid samples significantly increased the confidence interval of both the group index and GVD, particularly for wavelengths at the edge of the spectral range.

In Fig. 8(a), the scattering attenuation coefficient of Intralipid is shown as a function of wavelength for various volume fractions. Overall, the attenuation coefficient shows a monotonous decay with increasing wavelength. In this wavelength range, water absorption is negligible and the attenuation is caused solely by scattering. Also, Mie resonances are not visible in the spectra, as the sample is very polydisperse and the typical particle size 50–300 nm for Intralipid [24,36,47] is relatively small compared to the wavelength.

In Fig. 8(b), the volume fraction dependence of the attenuation coefficient is shown for various wavelengths. The effect of dependent scattering is clearly visible by a nonlinear increase in the attenuation coefficient. The volume fraction of maximum attenuation is 0.265 as obtained from the fit of Eq. (15). This is larger than the volume fraction of soy oil in undiluted Intralipid 20%. The data match well to literature values at wavelengths of 635 and 750 nm (Aernouts *et al.* [48]) and 800 nm (Kodach *et al.* [49]).

The attenuation data are fitted with Eq. (15). The proportionality constant is found to be $A = 1.57 \pm 0.01$, the wavelength dependence is given by the parameter $\alpha = 2.587 \pm 0.001$, and the packing dimension $p = 1.04 \pm 0.01$.

5. DISCUSSION

A. Refractive Index

This work not only provides the optical properties for separate wavelengths, but the broad range also results in a more accurate determination of the dispersive refractive properties with the quantification of the group index and GVD.

The measured group index for pure and dilutions of glycerol is slightly higher than reported in literature [41,50]. The GVD has a good match at the center wavelength, and for other wavelengths, there is a deviation that we attribute to the occurrence of fringes near the edges in the phase of the Hilbert transform.

The group index of pure ethanol is very close to the value determined by Kedenburg *et al.* [42]. For the ethanol dilutions, the effect of the volume contraction is slightly less prominent than predicted with Eq. (12) and the mass density as determined by Danahy *et al.* [44]. Similarly, the GVD is well predicted by the literature values.

Many authors [40–42,51] measure the refractive index for each wavelength separately and obtain the dispersion through a fit. Since the GVD is a sum of the first and second derivatives to the wavenumber of the refractive index, any choice of the dispersion equation or the presence of noise in the measured data points has a disproportional effect on the GVD. Therefore, literature values of the GVD vary wildly. The reported values of the GVD of glycerol at the wavelength of 589 nm range from 45.5 [41] to $68.1\ \mathrm{fs}^2\ \mathrm{mm}^{-1}$ [50]. We determined it at $72.4 \pm 0.5\ \mathrm{fs}^2\ \mathrm{mm}^{-1}$. For ethanol, reported values range from 55.1 [42] to $65.3\ \mathrm{fs}^2\ \mathrm{mm}^{-1}$ [52]. We determined it at $56.8 \pm 0.3\ \mathrm{fs}^2\ \mathrm{mm}^{-1}$. Both are close to, or well within, the range provided in literature.

Because the spectral phase is obtained close to a continuum of wavelengths, the dispersive properties could be fit more accurately. Therefore the method presented in this work would provide a method to accurately determine the GVD of a medium. To provide an accurate measurement of the GVD with other methods, for example, an Abbe refractometer, measurements at many wavelengths would be required.

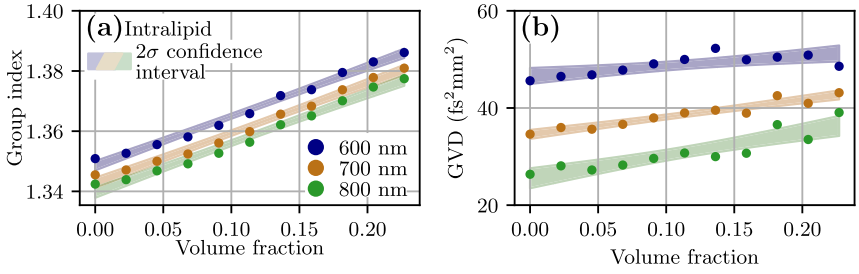

Fig. 7. (a) Group index of dilutions of Intralipid 20% as function of volume fraction for various wavelengths. (b) GVD of dilutions of Intralipid 20% as function of volume fraction for various wavelengths. The expected value is calculated by using the average refractive index weighted by volume fraction.

The spread in the datapoints of the group index and GVD of Intralipid as shown in Fig. 7 is much higher than the spread observed in the data of the transparent media. This is due to the lower transmission and the necessity to use a smaller flow channel size. For wider flow channels, the GVD can be more accurately determined, as the increased path length leads to more accumulated phase change. However, this would lead to very small signals at very high volume fractions.

B. Optical Attenuation

The wavelength dependent scattering attenuation shown in Fig. 8(a) generally matches the expected dependent scattering for Mie scatterers. The anomaly between 800 and 900 nm for undiluted Intralipid is caused by the lower response of the spectrometer for longer wavelengths, as can be seen from the water calibration measurement in Fig. 4(a). Here the measured intensity for wavenumbers lower than 7.5 μm^{-1} (840 nm) is very low for both the measurement and calibration.

The measured dependent scattering attenuation coefficient of Intralipid is similar to that reported in literature [12,36,47–49,53] for all wavelengths. The value of the wavelength dependence parameter in Eq. (15) $\alpha = 2.573 \pm 0.001$ compares well to values reported in literature. Reported values for α range from $\alpha = 2.40$ [53] to $\alpha = 2.59$ [48].

Although the attenuation spectra are similar, the obtained fitted packing dimension $p = 1.04 \pm 0.01$ is much lower. Since p parameterizes the volume fraction of minimum transmission, deviations at high volume fractions have a disproportional effect on the fit parameter p. Since the spread in the scattering attenuation data is higher at high volume fractions, the standard error in the estimate of p from the fit is probably not representative of the uncertainty. This value also differs significantly from the value reported by Aernouts *et al.* [48] who found p to be between 1.55 and 2.02, depending on wavelength. The value of p as determined in this work would give the volume fraction of maximum attenuation at $f_v = 0.28$, which is higher than the volume fraction of 0.227 of soy oil in pure Intralipid 20 %. A measurement of denser Intralipid samples would improve the estimate of p.

This value of p gives an indication of the shape of the scatterers or the size polydispersity. Since the shape of the soy oil globules is not expected to deviate much from a spherical shape [48], it is also possible to attribute the difference in packing dimension to a difference in particle size distribution of the Intralipid sample. This may be caused by differences in particle size between Intralipid batches or due to a different shelf time.

C. Spectral Interferometric Sensing

For sensing applications, measurement of the mixing ratio of the glycerol and Intralipid dilutions through the group index or GVD is straightforward, as both are monotonously increasing functions. The mixing ratio of ethanol–water mixtures is more difficult to determine because the group refractive index has a maximum at 75 vol.% and therefore cannot be uniquely determined in the range of 50–100 vol.%. The GVD is both measured and predicted to monotonically increase with the mixing ratio at 800 nm. Measuring the GVD at this wavelength provides an opportunity to overcome the ambiguity in the group index measurement.

The attenuation coefficient, group index, and GVD were extracted from a single measured interference signal. This makes this method particularly suitable for use as an on-chip implementation where the spectrum of the sample arm and reference arm cannot be measured separately. A similar approach is also used in an on-chip application by Zhou *et al.* [29]. Alternatively, when higher accuracy is required, both the sample arm and reference arm intensities can be measured separately. This can avoid spatial domain filtering, which decreases the spectral resolution and leads to artifacts that result from the filtering. For phase measurement, the independent measurement of the background intensities decreases the fringe patterns at the edges of the spectrum. However, for attenuation coefficient measurements, homodyne detection offers increased sensitivity for opaque samples.

6. CONCLUSION

In this paper, a method is presented to simultaneously measure the group index, GVD, and attenuation coefficient over a broad wavelength range between 400 and 920 nm for glycerol and

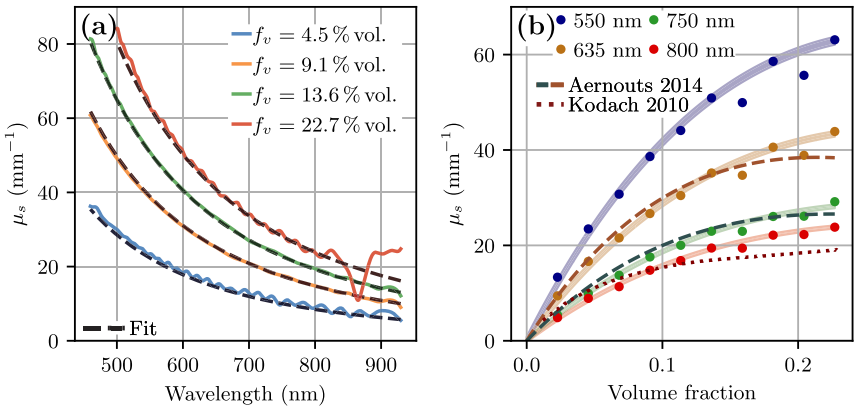

Fig. 8. (a) Attenuation coefficient of Intralipid as function of wavelength for various volume fractions. Fits are with Eq. (15). (b) Scattering coefficients for various wavelengths. The effect of dependent scattering is clearly visible as a flattening of the scattering coefficient. Literature data from Aernouts and Kodach are shown at the same wavelength as the measurements.

ethanol and from 500 nm for undiluted Intralipid. All three quantities are obtained from a single calibrated interference spectrum. All quantities are found to be similar to what is reported in literature.

Funding. Nederlandse Organisatie voor Wetenschappelijk Onderzoek (P17-24 project 6).

Acknowledgment. We thank Ron Hoogerheide for technical support.

Disclosures. The authors declare no conflicts of interest.

Data availability. Data underlying the results presented in this paper and the relevant analysis routines are available in Ref. [54].

REFERENCES

1. P. Bouguer, *Essai D'Optique, Sur La Gradation De La Lumiere* (Claude Jombert, 1729).
2. C. Veenstra, A. Lenferink, W. Petersen, W. Steenbergen, and N. Bosschaart, "Optical properties of human milk," Biomed. Opt. Express **10**, 4059–4074 (2019).
3. N. Bosschaart, G. Edelman, and M. Aalders, "A literature review and novel theoretical approach on the optical properties of whole blood," Lasers Med. Sci. **29**, 453–479 (2014).
4. J. Trevathan, W. Read, and S. Schmidtke, "Towards the development of an affordable and practical light attenuation turbidity sensor for remote near real-time aquatic monitoring," Sensors **20**, 1993 (2020).
5. A. Postelmans, B. Aernouts, J. Jordens, T. van Gerven, and W. Saeys, "Milk homogenization monitoring: Fat globule size estimation from scattering spectra of milk," Innov. Food Sci. Emerging Technol. **60**, 102311 (2020).
6. R. H. Sagor, M. F. Hassan, A. A. Yaseer, E. Surid, and M. I. Ahmed, "Highly sensitive refractive index sensor optimized for blood group sensing utilizing the Fano resonance," Appl. Nanosci. **11**, 521–534 (2021).
7. S. K. Chamoli, S. C. Singh, and C. Guo, "Design of extremely sensitive refractive index sensors in infrared for blood glucose detection," IEEE Sens. J. **20**, 4628–4634 (2020).
8. J. Chen, W. Guo, M. Xia, W. Li, and K. Yang, "In situ measurement of seawater salinity with an optical refractometer based on total internal reflection method," Opt. Express **26**, 25510–25523 (2018).
9. S. M. Bagherzadeh, B. Grajciar, C. K. Hitzenberger, M. Pircher, and A. F. Fercher, "Dispersion-based optical coherence tomography oct measurement of mixture concentrations," Opt. Lett. **32**, 2924–2926 (2007).
10. A. K. Trull, J. van der Horst, J. G. Bijster, and J. Kalkman, "Transmission optical coherence tomography based measurement of optical material properties," Opt. Express **23**, 33550–33563 (2015).
11. Y. Park, T. Yamauchi, W. Choi, R. Dasari, and M. S. Feld, "Spectroscopic phase microscopy for quantifying hemoglobin concentrations in intact red blood cells," Opt. Lett. **34**, 3668–3670 (2009).
12. B. Aernouts, E. Zamora-Rojas, R. V. Beers, R. Watté, L. Wang, M. Tsuta, J. Lammertyn, and W. Saeys, "Supercontinuum laser based optical characterization of Intralipid phantoms in the 500-2250 nm range," Opt. Express **21**, 32450–32467 (2013).
13. S. Korposh, S. W. James, S.-W. Lee, and R. P. Tatam, "Tapered optical fibre sensors: current trends and future perspectives," Sensors **19**, 2294 (2019).
14. I. Brice, K. Grundsteins, K. Draguns, A. Atvars, and J. Alnis, "Whispering gallery mode resonator temperature compensation and refractive index sensing in glucose droplets," Sensors **21**, 7184 (2021).
15. A. Ksendzov and Y. Lin, "Integrated optics ring-resonator sensors for protein detection," Opt. Lett. **30**, 3344–3346 (2005).
16. H.-Y. Lin, C.-H. Huang, G.-L. Cheng, N.-K. Chen, and H.-C. Chui, "Tapered optical fiber sensor based on localized surface plasmon resonance," Opt. Express **20**, 21693–21701 (2012).
17. W. Calhoun, H. Maeta, S. Roy, L. Bali, and S. Bali, "Sensitive real-time measurement of the refractive index and attenuation coefficient of milk and milk-cream mixtures," J. Dairy Sci. **93**, 3497–3504 (2010).
18. M. K. Dong, K. G. Goyal, B. Worth, S. Makkar, W. R. Calhoun, III, L. M. Bali, and S. Bali, "Accurate in situ measurement of complex refractive index and particle size in Intralipid emulsions," J. Biomed. Opt. **18**, 087003 (2013).
19. H. Contreras-Tello and A. García-Valenzuela, "Refractive index measurement of turbid media by transmission of backscattered light near the critical angle," Appl. Opt. **53**, 4768–4778 (2014).
20. E. Gutiérrez-Reyes, A. Garía-Valenzuela, and R. G. Barrera, "Extension of Fresnel's formulas for turbid colloidal suspensions: a rigorous treatment," J. Phys. Chem. B **118**, 6015–6031 (2014).
21. G. H. Meeten, "Refractive index errors in the critical-angle and the Brewster-angle methods applied to absorbing and heterogeneous materials," Meas. Sci. Technol. **8**, 728–733 (1997).
22. H. Liu, J. Ye, K. Yang, M. Xia, W. Guo, and W. Li, "Real part of refractive index measurement approach for absorbing liquid," Appl. Opt. **54**, 6046–6052 (2015).
23. N. Bosschaart, M. Aalders, D. Faber, J. Weda, M. van Gemert, and T. van Leeuwen, "Quantitative measurements of absorption spectra in scattering media by low-coherence spectroscopy," Opt. Lett. **34**, 3746–3748 (2009).
24. V. Kodach, D. Faber, J. van Marle, T. van Leeuwen, and J. Kalkman, "Determination of the scattering anisotropy with optical coherence tomography," Opt. Express **19**, 6131–6140 (2011).
25. V. D. Nguyen, D. J. Faber, E. van der Pol, T. G. van Leeuwen, and J. Kalkman, "Dependent and multiple scattering in transmission and backscattering optical coherence tomography," Opt. Express **21**, 29145–29156 (2013).
26. B. Ghafaryasl, K. A. Vermeer, J. Kalkman, T. Callewaert, J. F. de Boer, and L. J. van Vliet, "Attenuation coefficient estimation in Fourier-domain OCT of multi-layered phantoms," Biomed. Opt. Express **12**, 2744–2758 (2021).
27. C. Photiou and C. Pitris, "Comparison of tissue dispersion measurement techniques based on optical coherence tomography," J. Biomed. Opt. **24**, 046003 (2019).
28. S. M. Kolenderska, B. Bräuer, and F. Vanholsbeeck, "Dispersion mapping as a simple postprocessing step for Fourier domain optical coherence tomography data," Sci. Rep. **8**, 9244 (2018).
29. C. Zhou, M. K. Hedayati, and A. Kristensen, "Multifunctional waveguide interferometer sensor: simultaneous detection of refraction and absorption with size-exclusion function," Opt. Express **26**, 24372–24383 (2018).
30. D. Reolon, M. Jacquot, I. Verrier, G. Brun, and C. Veillas, "High resolution group refractive index measurement by broadband supercontinuum interferometry and wavelet-transform analysis," Opt. Express **14**, 12744–12750 (2006).
31. J. van der Horst, A. K. Trull, and J. Kalkman, "Deep-tissue label-free quantitative optical tomography," Optica **7**, 1682–1689 (2020).
32. A. Cauchy, *Mémoire sur la dispersion de la lumière* (J. G. Calve, 1836).
33. J. B. Biot and D. F. Arago, "Sur les affinités des corps pour la lumière, et particulièrement sur les forces réfringentes des différens gaz," Mémoires l'Académie sciences l'Institut France **6**, 301–387 (1806).
34. L. Lorenz, "Experimentale og theoretiske undersøgelser over legemernes brydningsforhold," Det K. Dan. Vidensk. Selsk. Skr. **5**, 483–518 (1875).
35. H. Lorentz, *Over het verband tusschen de voortplantingssnelheid van het licht en de dichtheid en samenstelling der middenstoffen*, Vol. **18** of Verhandelingen der Koningklijke Academie van Wetenschappen (1879).
36. H. J. van Staveren, C. J. M. Moes, J. van Marie, S. A. Prahl, and M. J. C. van Gemert, "Light scattering in Intralipid-10% in the wavelength range of 400–1100 nm," Appl. Opt. **30**, 4507–4514 (1991).
37. V. Twersky, "Transparency of pair-correlated, random distributions of small scatterers, with applications to the cornea," J. Opt. Soc. Am. **65**, 524–530 (1975).
38. P. A. J. Bascom and R. S. C. Cobbold, "On a fractal packing approach for understanding ultrasonic backscattering from blood," J. Acoust. Soc. Am. **98**, 3040–3049 (1995).

39. P. Virtanen, R. Gommers, T. E. Oliphant, *et al.*, "SciPy 1.0: Fundamental algorithms for scientific computing in python," Nat. Methods **17**, 261–272 (2020).
40. M. Daimon and A. Masumura, "Measurement of the refractive index of distilled water from the near-infrared region to the ultraviolet region," Appl. Opt. **46**, 3811–3820 (2007).
41. V. Gupta, O. Aftenieva, P. T. Probst, S. Sarkar, A. M. Steiner, N. Vogel, A. Fery, and T. A. F. König, "Advanced colloidal sensors enabled by an out-of-plane lattice resonance," Adv. Photon. Res. **3**, 2200152 (2022).
42. S. Kedenburg, M. Vieweg, T. Gissibl, and H. Giessen, "Linear refractive index and absorption measurements of nonlinear optical liquids in the visible and near-infrared spectral region," Opt. Mater. Express **2**, 1588–1611 (2012).
43. A. Volk and C. Kähler, "Density model for aqueous glycerol solutions," Exp. Fluids **59**, 75 (2018).
44. B. B. Danahy, D. L. Minnick, and M. B. Shiflett, "Computing the composition of ethanol-water mixtures based on experimental density and temperature measurements," Fermentation **4**, 72 (2018).
45. K. Mizuno, Y. Miyashita, Y. Shindo, and H. Ogawa, "NMR and FT-IR studies of hydrogen bonds in ethanol-water mixtures," J. Phys. Chem. **99**, 3225–3228 (1995).
46. H. Ren, S. Xu, Y. Liu, and S.-T. Wu, "Liquid-based infrared optical switch," Appl. Phys. Lett. **101**, 041104 (2012).
47. M. Raju and S. N. Unni, "Concentration-dependent correlated scattering properties of Intralipid 20% dilutions," Appl. Opt. **56**, 1157–1166 (2017).
48. B. Aernouts, R. Watté, R. V. Beers, F. Delport, M. Merchiers, J. D. Block, J. Lammertyn, and W. Saeys, "Flexible tool for simulating the bulk optical properties of polydisperse spherical particles in an absorbing host: experimental validation," Opt. Express **22**, 20223–20238 (2014).
49. V. Kodach, N. Bosschaart, J. Kalkman, T. G. van Leeuwen, and D. J. Faber, "Concentration dependent scattering coefficients of Intralipid measured with OCT," in *Biomedical Optics and 3-D Imaging* (Optica Publishing Group, 2010), paper BSuD11.
50. J. Rheims, J. Köser, and T. Wriedt, "Refractive-index measurements in the near-ir using an abbe refractometer," Meas. Sci. Technol. **8**, 601–605 (1997).
51. P. R. Cooper, "Refractive-index measurements of liquids used in conjunction with optical fibers," Appl. Opt. **22**, 3070–3072 (1983).
52. P. Kozma, F. Kehl, E. Ehrentreich-Förster, C. Stamm, and F. F. Bier, "Integrated planar optical waveguide interferometer biosensors: A comparative review," Biosens. Bioelectron. **58**, 287–307 (2014).
53. R. Michels, F. Foschum, and A. Kienle, "Optical properties of fat emulsions," Opt. Express **16**, 5907–5925 (2008).
54. P. Speets and J. Kalkman, "Measuring optical properties of clear and turbid media with broadband spectral interferometry—data and analysis," Zenodo, 2023, https://doi.org/10.5281/zenodo.7838373.